INT. J. NUM. METH. HEAT FLUID FLOW, VOL. 4, 425–445 (1994)

COMPUTATIONAL INVESTIGATION OF COBRA PROBE OPERATION

M. M. DE GUZMAN, C. A. J. FLETCHER† AND J. D. HOOPER‡

†*Centre for Advanced Numerical Computation in Engineering and Science (CANCES), Mechanical Engineering Building, The University of New South Wales, Sydney, 2052, Australia*
‡*CSIRO Division of Mineral and Process Engineering, Lucas Heights, NSW 2234, Australia*

ABSTRACT

The detailed flow behaviour around a four-hole Cobra Pitot pressure probe, developed by the Commonwealth Scientific and Industrial Research Organization, Australia, (CSIRO), to determine the pressure and the velocity components in three dimensional single-phase/multi-phase fluid flow, is investigated computationally. The incompressible steady state Navier–Stokes equations are solved numerically using a general purpose computational fluid dynamics (CFD) code developed at CANCES. Computational results are presented for representative probe pitch and yaw angles at a Reynolds number $= 2 \times 10^3$, emphasising the pressure distribution and flow separation patterns on the probe tip adjacent to the pressure ports. Quantitative comparison of the computational simulation to experimental results is done by comparing experimental calibration data to numerically computed pressure responses. The topological features of the near tip flow behaviour are visualised using critical point concepts and three dimensional streamlines. Additional qualitative comparison to experiment is discussed using data from a preliminary experimental investigation using surface oil film visualisation techniques, where available. Conclusions are drawn concerning the near tip flow behaviour, the good level of agreement between the numerical results and experimental data and the effectiveness of using a computational analysis to provide accurate detail useful for engineering design purposes.

KEY WORDS Multihole pressure probes Computational fluid dynamics Finite volume

INTRODUCTION

The use of CFD (computational fluid dynamics) codes in industrial flows is now widely accepted as being a cost effective and time efficient alternative to more traditional methods of fluid flow investigation such as experimental measurements and theoretical analysis[1]. Modern engineering designs of fluid flow components usually involve complex geometries, turbulent flow and multiple phases. The high cost and technical difficulties associated with physical simulations or full scale experiments on prototypes are reasons why computational modelling is being more widely used in product design and analysis. In a computational simulation the complete fluid behaviour becomes known down to the scale of the computational grid mesh. This paper demonstrates the capabilities of CFD by examining in detail the flow behaviour around a device which itself is used to gather experimental fluid measurements, namely a multi-hole pressure probe. Typically, an experimental apparatus obtains valuable information about the overall flow from only a few measurements, for example, a four-hole pressure probe provides only four discrete pressure readings. In contrast a computational simulation has the capability, subject to the accuracy of the turbulence model, of providing predictions of all the relevant variables such as velocity,

0961–5539/94/040425–21$2.00

Received March 1993
Revised October 1993

pressure and turbulence intensity throughout the domain of interest, without the disturbance caused by the probe itself[2]. This capability makes a computational approach suitable for engineering design purposes. Knowing the flow behaviour at all points, and having the ability to vary any aspect (geometrical or otherwise) of the apparatus, makes it possible for the designer to investigate proposed changes quickly and efficiently. It therefore becomes economically feasible to produce an optimized design, because there is no need to build a large number of prototypes. Since the flow behaviour is coupled throughout the domain, the availability of the detailed computational predictions allows the confirming physical prototype measurements to be kept to a minimum.

To provide some background information on the usefulness of multi-hole pressure probes some well known measurement techniques are discussed briefly. The experimental measurement of mean fluid flow quantities can be carried out by several well known apparatus, such as laser Doppler velocimeters (LDV), hot wire probes and multi-hole pressure probes. Each has advantages and difficulties associated with their usage. The laser Doppler velocimeter is a non-contact system which can be used in highly turbulent flows[3]. Coherent laser beams intersect to form a measurement ellipsoid, through which the velocity of a light scattering particle can be measured. It has the disadvantages of extremely high capital cost, and difficulty in seeding the flow. It has problems in bias of more probable detection of higher velocity particles[4], and problems of spatial resolution in high subsonic and supersonic flows. Current LDV apparatus are too expensive, lack robustness, and are generally too bulky to be used in anything other than in experimental laboratory work. A promising area of work being undertaken by the CSIRO is the development of a particle image velocimetry (PIV) technique[5–6] which is a more robust technique than LDV and provides field rather than point velocity information.

The hot-wire anemometer is another experimental device for measuring the mean fluid flow quantities[7]. It is a lot less bulky than the LDV, and has a lower capital cost compared to the LDV by a factor of ten. It can very reliably measure the mean velocity and the Reynolds stresses as demonstrated by Hooper[8]. It is available in multi-sensor probe designs to resolve the total velocity vector within a cone angle of up to 30 degrees. It has several disadvantages, namely probe fragility and non-linearity of response at low flow velocities. There is also the calibration drift caused by contamination of the probe, mechanical damage to the probe surface and changes in ambient temperature. The extreme fragility of the hot-wire probe precludes its successful usage in industrial type flow situations.

The use of multi-hole Pitot pressure probes has shown them to be a robust and highly portable experimental measurement system, being very suitable for use in both laboratory and industrial situations, at moderate capital cost. Multi-hole pressure probes are used to measure fluid static and total pressure, along with the mean fluid velocity and direction[9]. Several probe geometries have been used to measure three-dimensional flows, including hemispherical and spherical shaped probes[10], and conical tip probes[11–12]. The number of pressure holes on the probe tip varies, with Wright[10] using five holes and Everett and co-workers[12] working with a seven hole probe. A common configuration is a five hole pressure probe, composed of five tubes interconnected to form a solid tip. In order to minimise the flow disturbance, the probes are made relatively small, with five-hole pressure probes usually around 2 to 3 mm in diameter. Ligrani *et al.*[13] discusses miniature five-hole pressure probes with tip diameters of about 1.22 mm, used in small confined areas and where the scales of turbulence are also small. Research undertaken by the CSIRO[14] concerning the frequency response of the coupled pressure transducer, pressure lines and probe orifices shows that both the larger scale turbulent structure and the total mean velocity vector of a flow can be determined by a multi-hole pressure probe. A more recent development is the use of a four-hole pressure probe to simultaneously measure the mean and fluctuating turbulent velocity components, along with the mean and dynamic component of the static pressure, at a point in a turbulent flow up to a frequency of 1.5 kHz[15]. The LDV and hot-wire anemometer cannot measure simultaneously the local mean and fluctuating pressure. Hooper *et al.*[15] have used, as an example, the measurement of the turbulent flow in a swirling jet to

demonstrate the capabilities of this high frequency pressure probe. The experimentally measured time record of the turbulent velocity components and static pressure in principle permits the calculation of any moments of these components, subject to the spatial and temporal resolution of the probe. The experimental system will facilitate testing of computational turbulence models.

The particular probe to be investigated in this paper is the four-hole Cobra pressure probe originally proposed by Shepherd[16]. This probe has a tip shaped like the frustrum of a pyramid, *Figure 1*. Three side holes surround a fourth central hole, with the three side faces ground flat to 45 degrees. The shaft has a 'J' configuration that maintains the probe tip at a fixed point whilst rotating about the shaft axis. Shepherd also discusses the relative merits of the four-hole Cobra probe as opposed to using five or more pressure ports. A four-hole probe has advantages over a five-hole probe in that less measurements need to be made during calibration and operation, less pressure readings are required, no redundant information is present, and a simpler, smaller probe can be manufactured. Only four independent pressure readings are needed since there are only four independent quantities to be measured: pressure, velocity, and two flow direction angles. *Figure 2* shows the front view of the probe tip, showing the central port on the central face, and the three side faces containing the three side ports. The three side faces are angled away from the central face at 45 degrees to give maximum angular sensitivity at small incidence angles. The four pressure ports or tappings are labelled *A*, *B*, *C* and *O*. One can appreciate the small scale that the computational model represents by these large circles indicating the pressure tappings. The positive location of flow separation at the edges of the pressure faces as a result of using a pyramidal shaped tip rather than a spherical or ellipsoidal tip, insures minimal sensitivity to Reynolds number variation[9].

Two measurement techniques are usually employed in the use of such probes. One is to orient the probe until the readings on opposite side holes are balanced, thus indicating the flow direction. This is referred to as null-balancing or nulling. Another technique is to fix the position of the probe, with the flow direction, velocity and pressure being calculated from the various hole pressures using calibrated data. Some probes use a combination of the two techniques, and the advantages and disadvantages of each are discussed by Bryer and Pankhurst[9]. The Cobra probe, under study here, measures flow quantities using a calibration technique. Extensive calibration data has been generated for this probe, its usage extending to flows up to 110 m/s, up to a yaw and pitch angle range of ± 48 degrees[17]. In this paper it was shown that the pressure response of the Cobra probe was insensitive to Reynolds number variation up to this high velocity. Hooper and Musgrove[17] also demonstrated the use and effectiveness of the probe in a typical industrial flow situation, namely in a highly turbulent wake region, and the feasibility of manufacturing the probe as a low cost, portable measuring system for industrial type flows.

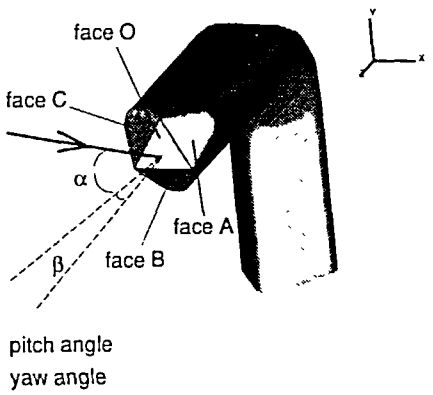

Figure 1 Cobra pressure probe and flow angles

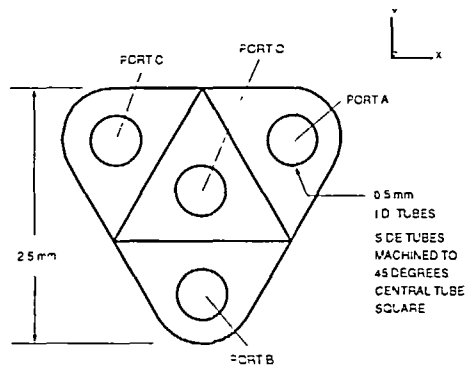

Figure 2 Front view of probe tip showing pressure ports

The aim of this paper is to study the detailed flow behaviour around the multi-hole Cobra probe computationally. The main objectives are:

(1) to perform Navier–Stokes computations of the three dimensional flow around such a probe at various pitch and yaw angles using a finite volume numerical scheme;
(2) to demonstrate the capability of the numerical methods to capture the detailed solution of the flow by quantitatively comparing the results to experimental calibration data and qualitatively comparing the results to available oil film visualisation results; and
(3) to investigate the various flow structures, separation, vortex formation and surface pressure distributions as a function of pitch and yaw angles by detailed examination of the computed flows.

The CFD code to be used is described below, with emphasis on the fact that this code is a very general piece of software that can solve a large variety of industrial type flows. An outline of the procedures employed in generating the computational grid will also be given. Detailed discussion of the computational results then follows.

COMPUTATIONAL FLUID DYNAMICS

The flow around a pyramidal shaped multi-hole probe even at low angles of orientation and low Reynolds number features complicated flow separation behaviour and vortices, with viscous effects playing a major role on the flow structure. An accurate numerical prediction of the flow requires the solution of the incompressible Navier–Stokes equations. The fluid flow around the probe is solved using a CFD code, RANSTAD (Reynolds Averaged Navier Stokes Solver for Aerodynamic Design). RANSTAD was developed for complex industrial flows, and is suitable for laminar or turbulent flows, in 2-D or 3-D. It handles both incompressible and compressible flows, and can also solve for temperature, enthalpy and two-phase behaviour[18]. It can solve for internal flows such as through ducts, coal classifiers and spin driers, and external flows, i.e. around wing body junctions, automobiles and buildings. RANSTAD uses a k–ε turbulence model to provide the Reynolds stress predictions[19]. A one- or two-layer wall function[20] is implemented with these models to avoid the need for very fine grids adjacent to solid surfaces. A higher order finite volume discretisation scheme[21] with inbuilt limiters combines robustness with higher-order accuracy on relatively coarse grids. Two phase flow simulations are modelled using an Eulerian formulation[22].

The code uses a non-orthogonal boundary fitted coordinate grid system[23]. The momentum equations are solved for the velocity components on a non-staggered grid, i.e. all variables U, V, W, P are stored at the centroids of the mass control volumes. The velocity components in fixed Cartesian directions are treated as scalars after the transformation from physical coordinates to computational space coordinates. Because of this the discretisation procedure can be illustrated using the scalar advection-diffusion equation as a prototype equation to be solved[2]. Writing it in Cartesian coordinates gives:

$$\frac{\partial}{\partial x_i}(\rho U^i \phi) = \frac{\partial}{\partial x_i}\left(\Gamma \frac{\partial \phi}{\partial x_i}\right) + S \tag{1}$$

or in a more convenient form,

$$\frac{\partial F_i}{\partial x_i} = S \tag{2}$$

where F_i the total (convective + diffusive) flux is given by:

$$F_i = \rho U_i \phi - \Gamma \frac{\partial \phi}{\partial x_i} \tag{3}$$

Equation (2) is discretised using a control volume formulation in generalised coordinates space, wherein the control volume is a unit cube. The metric information needed to relate the physical coordinate system to the computational space system is represented by area vectors[24], giving:

$$\sum_{n=1}^{6} F_n \cdot \mathbf{A}_n = V_c \langle S \rangle \tag{4}$$

where $\mathbf{A}_n$ is the area vector corresponding to the nth face of the control volumes in physical space. V_c is the actual volume of the control volume in physical space.

First order derivatives in the governing equations are evaluated using four-point asymmetric discretisation[24] to retain high accuracy on coarse grids. Second derivatives are evaluated using three-point symmetric formulae. Each governing equation is sequentially relaxed to update one of the primitive variables. A velocity potential correction is introduced to satisfy continuity and upgrade the pressure using a modified SIMPLEC algorithm[25]. The Rhie–Chow[26] momentum interpolation method is used to prevent chequerboard oscillations in pressure and velocity, since using a non-staggered grid and centered differences can effectively decouple the odd and even grids. A strongly implicit procedure (SIP) scheme is used to upgrade the velocity components and the velocity potential.

Grid generation

The CFD code used to solve the 3-D fluid flow around this probe required a structured, single block grid[27] in a body fitted coordinate system. Single block meaning that the grid maps the entire physical domain onto a single computational box. Structured in the sense that grid point coordinates can be identified by increasing sequences of integers, i.e. there is a constant number of control volumes in each of the 3 spatial coordinate directions[28]. Therefore the computational grid is referred to as being topologically cuboidal. The 3-D grid is constructed by stacking 2-D grid surfaces, these surfaces being slices through the probe cross-sectional area. Stacking of surfaces have been used widely, i.e. in papers by Chang[29], Chen *et al.*[30], and Holst and Thomas[31]. Algebraic methods of grid generation are used to construct the individual 2-D grid surfaces. After stacking, the resulting 3-D grid is smoothed or refined by applying partial differential equations based on Laplace equations. These equations are one of the more common differential models used for grid coordinate generation[32].

On each 2-D slice, the multisurface method[33] is applied to twelve separate blocks or sections of the grid. In each block the multisurface method is used with two intermediate surfaces, one of which is adjacent to the probe surface to produce a grid which is locally near-orthogonal to the solid body. The bounding curves defining the domain and the solid surfaces are represented by Hermite splines[34] for ease of geometry specification. Grid point clustering near the solid surfaces is accomplished by distributing the points along the bounding curves using one-dimensional stretching functions. An example of a 2-D surface of the grid through the probe cross section is shown in *Figure 3a*.

After stacking the 2-D grid slices to form the 3-D grid, the existing grid has a large number of regions where grid overlap and highly skewed grid cells occur. This seems to be a common occurrence in 3-D grid generation methods, especially where 2-D grids are combined to form 3-D grids[35–36]. Here, the existing grid is improved in terms of smoothness and orthogonality by applying an elliptic generation system based on the Laplace equations[23,32]:

$$\nabla^2 \xi^i = 0 \qquad (i = 1, 2, 3) \tag{5}$$

Forsey[37], Jameson and Baker[38] have used elliptic grid generation systems to act as a smoother to an existing grid. The governing differential equations in physical coordinates are presented conveniently by Warsi[32]. They are:

$$Dx_i = 0 \tag{6}$$

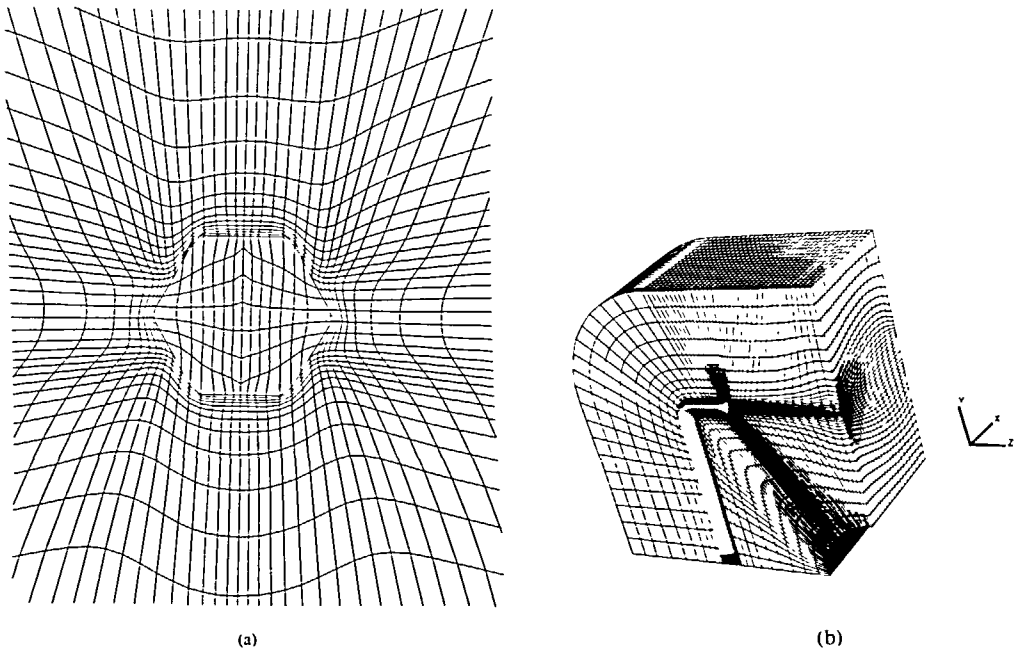

Figure 3 (a) A two-dimensional surface grid through the probe cross-section; (b) a three-dimensional grid (cut across symmetry plane)

where the operator D is given by:

$$D = G_1\partial_{\xi\xi} + G_2\partial_{\eta\eta} + G_3\partial_{\zeta\zeta} + 2G_4\partial_{\xi\eta} + 2G_5\partial_{\zeta\zeta} + 2G_6\partial_{\eta\zeta}$$

Here, use is made of the following quantities: $G_1 = g_{22}g_{33} - (g_{23})^2$, $G_2 = g_{11}g_{33} - (g_{13})^2$, $G_3 = g_{11}g_{22} - (g_{12})^2$, $G_4 = g_{13}g_{33}$, $G_5 = g_{12}g_{23} - g_{13}g_{22}$, $G_6 = g_{12}g_{13} - g_{23}g_{11}$, where g_{ij} are the covariant components of the metric tensor, i.e.:

$$g_{ij} = \sum_{k=1}^{3} \frac{\partial x^k}{\partial \xi^i}\frac{\partial x^k}{\partial \xi^j}$$

Equations (6) are discretised using centered-difference formulae[24], and a successive over-relaxation scheme (SOR) is used to solve the system of equations iteratively. Added control for the grid refinement is achieved by letting the SOR relaxation factor be a function of spatial position, since different degrees of smoothing and grid clustering are required at various parts of the computational domain. Discrete grid points, namely those representing the solid probe geometry have fixed positions. A sample grid is shown in *Figure 3b*.

Boundary conditions and grid resolution

Inlet Dirichlet boundary conditions of velocities are imposed on the windward side of the computational domain. The leeward control volumes have outlet pressure boundary conditions. Whether a control volume is an inlet or an outlet is governed as a function of the probe pitch and yaw angles relative to the flow. The probe itself is composed of solid control volumes except for the four pressure ports, in which the fluid behaviour inside are modelled to one diameter in depth. Zero flow Dirichlet boundary conditions are then placed at the bottom of these ports.

There are several possible sources of errors that can affect the accuracy of the solution when using a numerical computation. Two that are worth mentioning here are grid resolution and boundary condition errors. These two factors are very much inter-related in this investigation. The probe is a very complicated geometry, with the tip containing several angled facets and sharp edges that needs to be closely modelled. Therefore, sufficient grid points are necessary near the tip to accurately resolve the near wall flow behaviour. This includes the prediction of the separated flow which occurs are certain angles of orientation. On the other hand, a sufficiently large computational domain is necessary to correctly apply the appropriate far-field boundary conditions, free of any disturbance created by the probe. Since the computational memory requirements are fairly substantial there has been a compromise in the maximum number of grid points utilised in this calculation. The computed results have indicated so far that the computational grids that have been used are sufficient to predict the detailed velocity and pressure distributions around the probe, but certainly more accuracy will be achieved if the capability to add more grid points closer to the surface is obtained. Future computational investigations will, possibly, involve a composite grid/composite solution scheme, whereby a complete computational mesh around the probe tip is embedded in another complete computational mesh, with this larger mesh encompassing a larger domain of interest[39]. The larger, less refined, mesh can have boundary conditions imposed on it without the disturbance caused by the probe. The (time dependent) boundary conditions for the inner mesh is then provided by the current solution of the outer mesh at every iteration. This scheme will require far less computer memory than, say, merely doubling the number of grid points on the original large mesh. Increased accuracy will result due to the larger number of grid points clustered closer to the surfaces.

RESULTS

Two computational grids were used in the calculations. The first has $44 \times 39 \times 56$ grid cells, and the domain boundaries were at least 20 times the probe width away from the tip. The second has $44 \times 39 \times 57$ grid cells, and the domain boundaries were at least 7 times the probe width away from the tip. This second grid was used as the form of grid refinement, because increasing the number of grid points further was going to place too much of a burden on the computational memory requirements. The re-distribution and re-clustering of more grid points closer to the solid surfaces was done instead. The first grid was sufficient to confirm the results of the experimental calibration data, but the second grid, with a larger number of grid points clustered closer to the tip, gave better resolution of the detailed flow adjacent to the tip. The computations required approximately 900 global iterations to reduce the rms residuals to below 1×10^{-9}. The results that will be presented here correspond to the probe being immersed in a uniform freestream velocity of 16 m/s, with a Reynolds number of 2×10^3 based on the tip width. For this Reynolds number a laminar model is used. Turbulent cases have also been investigated using a k–ε turbulence model. The results for these turbulent cases also show good agreement with experimental calibration data, and the pressure distribution and flow patterns are not unlike the ones using a lower Reynolds number.

An appropriate way of verifying the computational results is by comparing them to the experimental calibration data for the probe. The experimental calibration procedure used by the CSIRO is described in greater detail by Hooper and Musgrove[17]. The pitch and yaw angle of the probe is varied in the range between ± 48 degrees. The probe tip was positioned in the potential core of an air jet formed from a pipe nozzle. Two pipe diameters were used, a 50 mm i.d. and an 80 mm i.d. pipe. The central jet region composed of one half of the pipe diameter showed less than 0.5% variation in the mean dynamic pressure when measured using radial traverses (using a hot wire probe). Data acquisition software is utilised to record the probe pressure responses using a dedicated personal computer. In actual usage of the probe in an

unknown flow the recorded data sets are interpolated to provide the magnitude and direction of the mean velocity vector and the local dynamic and static pressure.

The gross flow behaviour for various pitch and yaw angles of the probe are illustrated in *Figure 4*. In this figure the trajectories of massless particles injected into the flow is used as a visualisation aid. The flow is going from right to left. When the probe is facing head on to the flow, it has a pitch angle of zero and a yaw angle of zero, *Figure 4a*. A rotation along the shaft axis is represented by a change in yaw angle, *Figure 4b*. A tilt of the probe head corresponds to a change in pitch angle, *Figure 4c*. The general case is illustrated as a combination of pitch and yaw angles, *Figure 4d*.

The experimental calibration data is presented in the format of calibration charts as shown in *Figure 5*. Four pressure response surfaces (corresponding to the four pressure ports) are obtained as a function of the two variables pitch and yaw. The two dimensional curves shown in *Figure 5* represents a cut through these surfaces at a constant pitch angle. The horizontal axis shows the yaw angle increments. The vertical axis shows the non-dimensionalised pressure value, C_p. The four curves represent the pressure response of the four pressure ports as the yaw angle is varied, at a constant pitch angle. The computational investigation followed the format of these calibration charts. The solution of the fluid flow around the probe was solved for pitch and yaw angles varying in the range ± 48 degrees, in twelve degree increments. In *Figure 5*, the

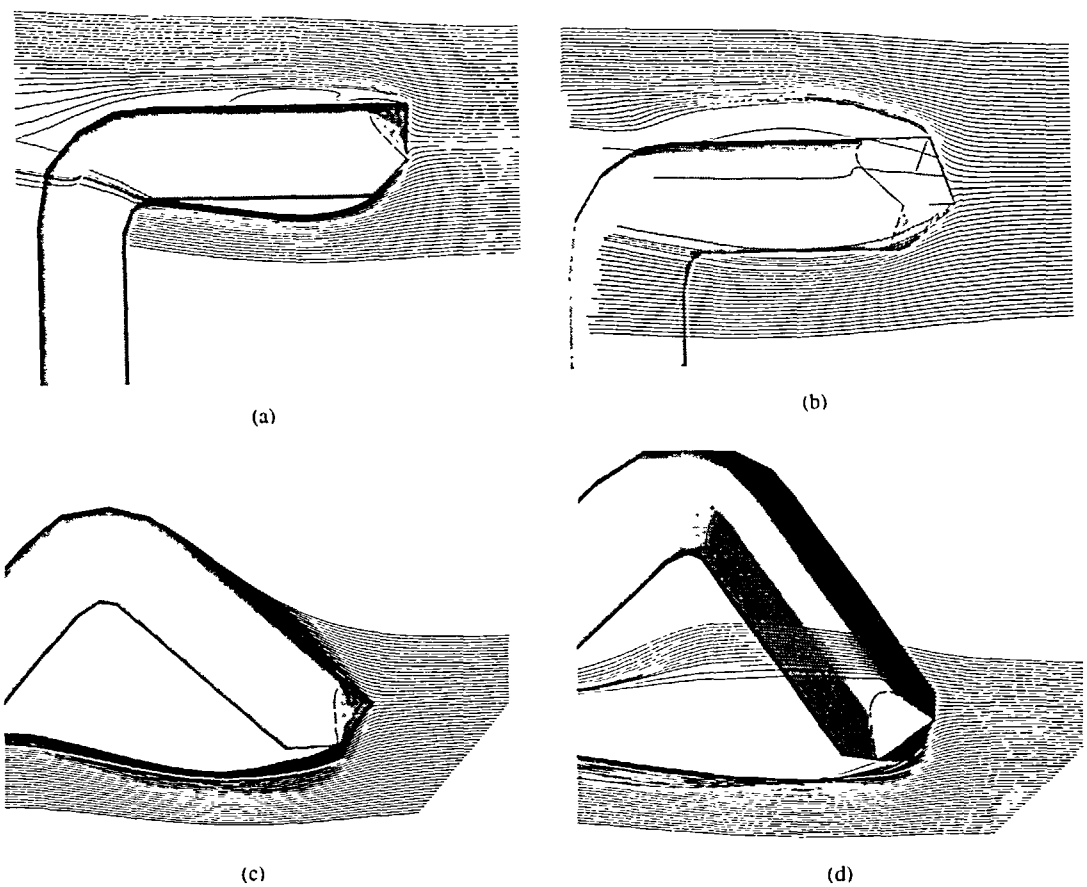

Figure 4 Streamline trajectories for different probe orientations. (a) Pitch = 0°, yaw = 0°; (b) pitch = 0°, yaw = 36°; (c) pitch = 42°, yaw = 0°; (d) pitch = 42°, yaw = 36°

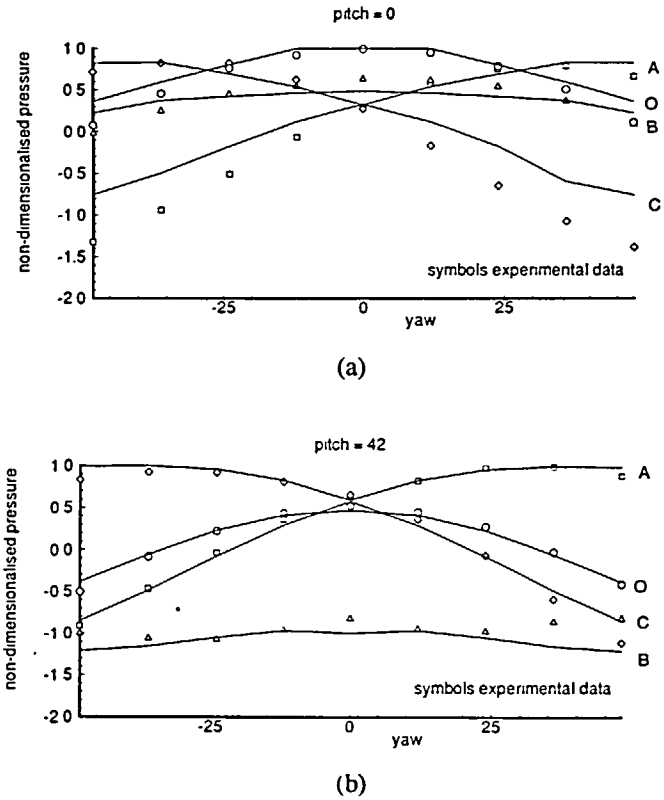

Figure 5 Calibration charts. (a) Pitch = 0°; (b) pitch = 42°

curves represented by solid lines are the computational results, and the symbols represent the experimental results. The labels *A*, *B*, *C* and *O* for the four pressure ports (see also *Figure 2*) identify the computational results (solid line curves). Since the pressure ports in the computational model are composed of several grid control volumes, the simplest way to calculate the pressure value was to average the individual cell values. It is seen that there is good overall agreement between the computations and the experiments. The discrepancies that occur do so at the higher values of pitch and yaw angles, and on the pressure ports that are on the leeward side faces with respect to the flow. For example, looking at *Figure 5a* it is seen that the discrepancies occur for pressure ports *A* and *C*. When the pitch angle is zero and the yaw angle is increased, these two pressure faces are oriented away from the direction of the flow. It is perhaps the local separation (that is, the more complicated wake region) that occurs on these faces that contribute to the inaccuracy of the comparison. Looking at *Figure 5b* a similar situation is evident in the readings for pressure port *B*, although the discrepancies here are not too significant. Port *B* is the leeward facing face when the pitch angle is increased to 42 degrees. Again it is surmised that the more complicated reversed flow regions on this face lead to the discrepancies between the experimental and computational results.

The following results will concentrate on the detailed flow at the probe tip. Going through the various pitch and yaw configurations present in the two calibration charts, various orientations of the probe will be used to illustrate the general flow patterns that occur around the probe tip. Some of these cases highlight fairly extreme conditions of pitch and yaw angles of the probe, including those which exhibit some discrepancies in the calibration chart comparisons.

In experimentally visualising the flow around three dimensional bodies and the interaction of the fluid with the surface of the body, use is often made of the surface oil film technique[40]. The body is coated with a special oil film, and flow patterns form on the surface when the body is exposed to an air flow due to the frictional forces which carry the oil along. The remaining oil pattern on the surface gives an indication of the behaviour of the flow. These patterns are useful in flow visualisation of three dimensional separated flow off solid surfaces. The exact composition of the oil mixture used in such experiments vary greatly in the available literature, but a combination the authors have utilised is kerosene, oleic acid, titanium dioxide and fluorescent powder[41]. The kerosene and oleic acid control the viscosity of the mixture, and the titanium dioxide and fluorescent powder provide the streak patterns. A preliminary experimental investigation, using such a technique, was undertaken at CSIRO. The experiments were done using a 5 to 1 larger prototype model of the probe, with the pressure ports temporarily blocked. The surface of the probe was coated with a smooth black paint finish to improve the visual resolution. The pipe nozzle used in the original calibration procedures was used to provide the uniform flow source. Due to the relative size scales involved, i.e. the size of the available model, the particle sizes of the titanium dioxide (0.2 microns), the experiments had to rely on a certain range of flow rate from the nozzle to produce reasonable streak patterns. Therefore, the experiments were carried out at a higher Reynolds number ($Re = 1 \times 10^4$) than the computations ($Re = 2 \times 10^3$). The technical considerations meant that several factors contributed to the experiments being slightly non-identical to the numerical simulations. The large probe prototype itself was of slightly different geometrical features at the probe shank and stem to the smaller probe models that were incorporated in the numerical modelling, although this should not affect the gross flow separation patterns adversely. The surface finish of the experimental model was another factor which should give little difference in the results between the computations and experiments. The Reynolds number variation was a factor which had to be considered when comparing the computational results to the experiments, since this affected critical details such as the point of separation. The handful of cases that have been done show very favourable agreement with the computational results, giving the authors increased confidence in the computational procedure.

The flow around the Cobra probe tip is characterised by three-dimensional flow separation, hence use is made here of computed surface particle pathlines to provide the computational *oil streaks*. The description of the flow behaviour using these streak patterns are facilitated by exploiting topological features following Perry and Chong[42], Tobak and Peake[43]. Their approach relies on treating the flow field as a continuous vector field, and identifying the location and type of so called singular or critical points. Here the interest is in the types of critical points that occur on the surface of a body, i.e. two dimensional critical points. These critical points are the prominent features of the three dimensional flow around the body, identifying the distinguishing characteristics of the flow. For example, a necessary condition for flow separation is the convergence of the oil streak lines onto a particular line. Chapman and Yates[44] state that the description of three dimensional flows using topological concepts requires the treatment of four areas:

(1) The types of critical or singular points that can occur in a two dimensional field.
(2) The global properties to which the patterns of these critical points must conform.
(3) The extension of the two dimensional critical points into the third dimension, such as in separated flow; and
(4) The use of bifurcation theory to describe the changes that can occur in the topological features.

Chapman and Yates gives an extensive review of these four concepts in their paper. Here, a brief description will be given only of the relevant areas which will assist in studying the flow around the probe.

Firstly the classification of critical points in a two dimensional vector field are reviewed. A

critical point is a point at which the magnitude of the vector is zero. In two dimensions, the critical points are classified into two main types, namely nodes and saddle points. Nodes are further classified into two sub-types, namely nodal points and foci. A nodal point is a point common to an infinite number of streak lines. A focus is where an infinite number of streak lines spiral around a singular point. A saddle point is characterised by two lines that intersect at a singular point. One of these has vectors directed at the singular point, the other has vectors directed away from the singular point. All other neighbouring lines miss the singular point and are asymptotic to these two lines, called 'separatrixes'.

Chapman and Yates present the mathematical reasoning why these two dimensional critical points (i.e. nodes, foci and saddle points) can lead to extensions into the flow off the surface, that is, into conclusions about three-dimensional critical points associated with two-dimensional critical points of the skin friction vector field on the surface. This then provides a means of understanding separation from the surface. When the streak lines are directed away from the nodal point, it is called a node of attachment, i.e. there is a vector trajectory from off the solid surface which pass through the critical point. When the streak lines are directed towards the nodal point, it is called a node of separation or detachment. Therefore there is a trajectory leaving the surface at that point. A node of attachment is usually a stagnation point on a forward facing surface of the body. A focus of attachment is one which spirals away from it, and a focus of separation is one which spirals into the singular point. In a saddle point, the vector lines near one of the separatrixes converge on that separatrix and it behaves in the manner of a line of separation. The vector lines near the other separatrix diverges from it and it behaves in the manner of a line of attachment.

Using global rules and properties that govern the relationship between the critical points when they occur on a surface of a body, one can establish a hypothesised description of the three-dimensional flow that occur around that body. For the purposes of this paper, only the identification and classification of the more interesting critical points will be attempted, since the probe as a whole is a complicated geometry with a large number of flow features that occur all the way around the probe shaft. An example of these flow features is the formation of leeward side vortices on the side of the probe which will be presented later in this paper, *Figure 12*. The important geometric features that will be examined closely are the pressure faces at the probe tip, since these directly influence the local flow behaviour and pressure readings. The calibration charts show that the leeward faces, those which have flow separation occurring, are the regions which show discrepancies in the pressure readings. Hence, only the flow patterns on the surfaces of the probe tip, in the vicinity of the pressure ports, will be presented. This will concentrate the discussion on the area of greatest importance, the pressure reading characteristics of the probe.

The first discussion centers on the onset of separated flow on the pressure faces at the probe tip as the inclination to the flow increased in small increments. The description of three dimensional separated flow behaviour is governed not only by the identification of the critical points, but also the manner in which these topological features originate and change from one form to another as the parameters of the flow is changed, for example changes in angle of attack, Reynolds number or geometry modifications. *Figures 6a* to *6e* illustrate the computational oil streak patterns calculated from the numerical flow solution as the pitch angle is kept at zero degrees and the yaw angle is increased from 0 to 48 degrees, in increments of 12 degrees. Recall that in this front view representation of the probe tip the three side faces are angled away from the central face at 45 degrees, see *Figure 2*. Therefore, as the yaw angle is increased face *A* turns into the flow (becomes the windward face) and face *C* increasingly becomes a leeward facing face, see *Figure 4b*. The arrows on the streak lines indicate the direction of the flow. *Figure 6a* shows the computational oil streaks on the faces of the probe tip for the case pitch = 0°, yaw = 0°. For this case, where the flow is hitting the probe straight on, a single node of attachment is seen, indicating the stagnation point of the flow. All streak lines originate from this node. The fluid then flows in a smooth, attached fashion towards the rear of the probe. No separation off the faces is yet apparent. The experimental surface oil streak pattern on the probe tip for

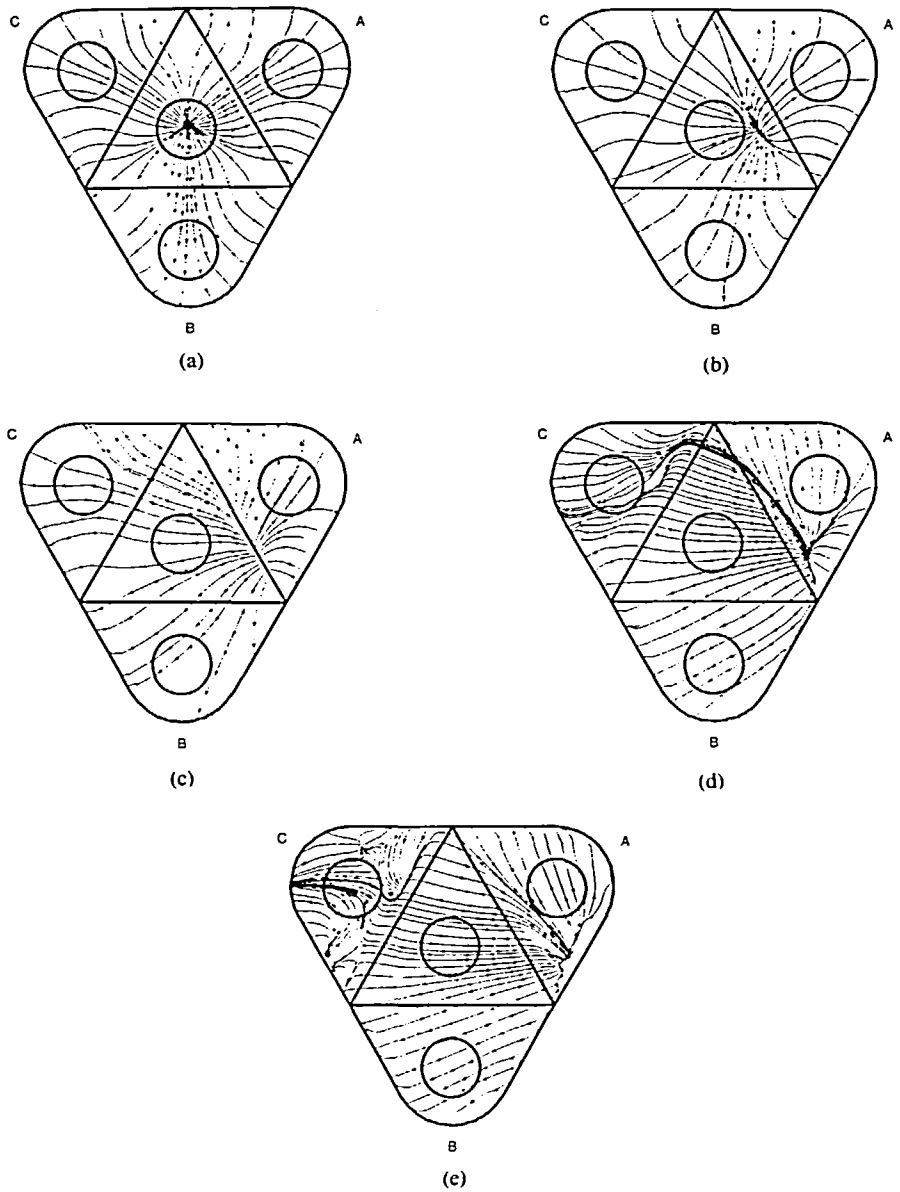

Figure 6 Computational phase portraits. (a) pitch = 0°, yaw = 0°; (b) pitch = 0°, yaw = 12°; (c) pitch = 0°, yaw = 24°; (d) pitch = 0°, yaw = 36°; (e) pitch = 0°, yaw = 48°

the case pitch = 0°, yaw = 0° has been examined by the authors, and is virtually identical to the computational pattern. The streak pattern has the distinct node clearly seen at the stagnation point. All the lines originate from this node, then flow in an attached fashion to the rest of the faces.

Tobak and Peake[43] espouse use structural stability and bifurcation theory to satisfactorily provide the flow description, while Chapman and Yates[44] also give a description of structural bifurcation theory. The pattern of streak lines on a surface such as in *Figure 6a* is called the phase portrait or the surface shear stress vector field. Two phase portraits have the same topological structure if a mapping from one phase portrait to another preserves the topological

structure (e.g. the number and types of critical points). A way to imagine such a preservation of structural structure is if the phase portrait is on a surface made of rubber sheeting. Then, any stretching of the surface without tearing or folding preserves the relevant singular or critical points. In defining structural stability, if a small change in the relevant flow parameters in a phase portrait which has the same topological structure as the previous one, then the phase portrait is said to be structurally stable. Increasing the yaw angle to 12 degrees, *Figure 6b*, does not alter the topological structure. The attachment node has merely shifted to the right. All streak lines originate from the one nodal point of attachment (i.e. the stagnation point) and continue on in an attached fashion around the faces. In *Figure 6c*, the yaw angle is further increased to 24 degrees, and still the flow is everywhere attached. The stagnation point has shifted more to the right, and is now at the edge between the faces. The topological features are still unchanged. Therefore the phase portrait has remained structurally stable so far.

As the yaw angle reaches 36 degrees the angle of attack reaches a point such that the flow develops instabilities on the leeward face, face *C*, *Figure 6d*. There is a distinction between structural stability and asymptotic stability of the flow. A flow has asymptotic stability if small perturbations from it decay to zero as time goes to infinity. Tobak and Peake[43] also distinguishes between local and global instabilities. A local instability does not alter the topological structure of either the phase portrait of the surface shear stress vector or the three dimensional velocity vector field. A global instability permanently alters both vector fields. If an (asymptotic) instability is one which does not alter the topological structure of the phase portrait then the convergence of streak lines onto one or several lines can only be a local event in the phase portrait, hence these particular lines are called local lines of separation. The leeward streak lines in *Figure 6d* tend to converge to a particular streak line. This particular line is labelled a local line of separation since the topological structure has remained unchanged, and the streaks are still emanating from the same attachment node.

When the yaw angle has reached 48 degrees the leeward flow has bifurcated to the portrait shown in *Figure 6e*. A (structural or asymptotic) instability which alters the phase portrait and changes the topological structure, resulting in the appearance of a saddle point in the streak patterns, is a global event in the phase portrait and hence the line emanating from the saddle point is labelled a global line of separation. Changes in the topological structure give rise to the notion of bifurcation. Structural bifurcations are those bifurcations that add critical points or change the structure of the critical points in the phase portrait. Bifurcations in the topological features can occur in three ways:

(1) new critical points appear;
(2) a critical point divides into multiple critical points; and
(3) critical points occur on a singular line due to a symmetry breaking structural bifurcation.

In *Figure 6e* the fluid still proceeds smoothly across the faces from the stagnation point until it hits face *C*. This face is very much on the leeward side of the body in this particular probe orientation. The attached streaklines converge onto a single line, which could be taken as evidence of flow separation. Beyond this *separation line* the streak patterns indicate reversed flow regions, with saddle points and a couple of lines which are asymptotic to other lines. This situation is classified as one of global separation, since the instabilities present in the flow have managed to alter the structural stability of the surface shear stress vector field to produce a different phase portrait than before. This case has been investigated using the experimental oil film technique. The streak lines on the windward side of the tip show an identical pattern, indicating the position of the attachment node. However, the patterns on face *C* are not as clearly distinguishable as the computational results, and a thin deposit of oil is seen just after the edge between face *C* and face *O*. This indicates that since the oil is not carried along by the fluid frictional forces, separation must have occurred right at the edge itself. This differs from the computations which indicate separation about a tenth of the way past the edge. This discrepancy could be due to the Reynolds number variation, since a lower Reynolds number in

the computations would allow the more laminar flow to remain attached to the surfaces further. The effects of numerical diffusion in the computational procedures could also serve to predict a slightly different separation point.

The preceding series of phase portraits on the probe tip, *Figures 6a–6e*, illustrates the flow patterns that occur during the calibration procedure that produced the chart in *Figure 5a*. It is seen that as the yaw angle becomes more severe, the flow patterns become more complex, with global separation starting to be present. Associated with this is the appearance of discrepancies between the computations and the experiments in *Figure 5a*. It is fairly clear that the computed pressure solution on the leeward faces (face *C* and face *A*) are slightly different to the experimentally measured pressure readings at these higher angles. Therefore, the accuracy of the solutions is most likely affected by the separated flow, and closer agreement should be achieved by increasing the accuracy of the computations by perhaps using a more refined grid mesh in the vicinity of the separation regions, than is possible here. The composite grid scheme mentioned earlier should be able to give increased accuracy in future investigations.

Shown in *Figures 7a* to *7e* are the phase portraits for a constant pitch angle of 42 degrees, with the yaw angle increasing from zero to forty-eight degrees in twelve degree increments. *Figure 7a* is the situation where starting from the pitch = 0°, yaw = 0° case (*Figure 6a*), the pitch angle was increased by tilting the probe downwards by 42 degrees. The stagnation point is indicated by the position of the attachment node in the upper part of face *O*. The flow goes smoothly downwards, then converges to a separation line (a line which other lines converge onto) on face *B*. For this probe orientation face *B* is the leeward face, see *Figure 4c*. A saddle point of separation and reverse flow regions are evident on this surface. The flow is clearly separating on this leeward face, with evidence of asymmetry in the flow pattern. This could be due to unsteadiness in the separated wake region. The phase portrait has changed from that of *Figure 6a*, bifurcation has occurred, therefore the topological structure has been altered and a situation of global separation exists. The experimental oil streak pattern for this case pitch = 42°, yaw = 0° shows that the oil film mixture has gathered in a thin strip just after the edge joining face *O* and face *B*. Since the oil film is not being carried along by the frictional shear forces then it can be concluded that the flow has separated at this point. The computational results predicts the separation point to be slightly more to the leeward side of face *B*, further down from the sharp edge. Beyond this separation region the pattern is not as clearly discernible. Again the Reynolds number variation between the computations and experiments probably contribute to the difference in the point of separation, as well as the effects of numerical diffusion. The experiments, corresponding to the higher Reynolds number, indicate a separation pattern occurring nearer to the sharp edge which is the expected trend. The experimental oil film steaks on faces *O*, *A* and *C* do show an identical pattern to the computational results.

Figure 7b shows the phase portrait after an increase in yaw angle by 12 degrees. The attachment node has shifted slightly to the right, and the streaks still flow in a smooth attached fashion along faces *O*, *A* and *C*. Face *B* still exhibits the line where all the other lines converge onto. The saddle point has shifted slightly to the right. There is a nodal point of detachment to the left of the saddle point which was not apparent in *Figure 7a*, so that the appearance of this critical point signifies a bifurcation of the phase portrait. Reversed flow is clearly occurring on face *B*. *Figure 7c* (pitch = 42°, yaw = 24°) exhibits an unchanged phase portrait after increasing the yaw angle. The phase portrait has remained stable since no changes in the topology has occurred. The node of attachment or stagnation point has moved slightly to the right as a consequence of the increase in yaw angle. The flow is still attached on faces *O*, *A* and *C*. Face *B* still has the topological features of a node (of detachment) and a saddle point. The node has moved to be just above the saddle point. This node-saddle point combination on face *B* is a clear sign of flow separation on this face. Increasing the yaw angle to 36 degrees, *Figure 7d*, does not alter the stability of the phase portrait. Exactly the same topological features are displayed, with only a minor shifting in the placement of the critical points evident.

Eventually, the increase in yaw angle results in breaking the stability of the portraits and

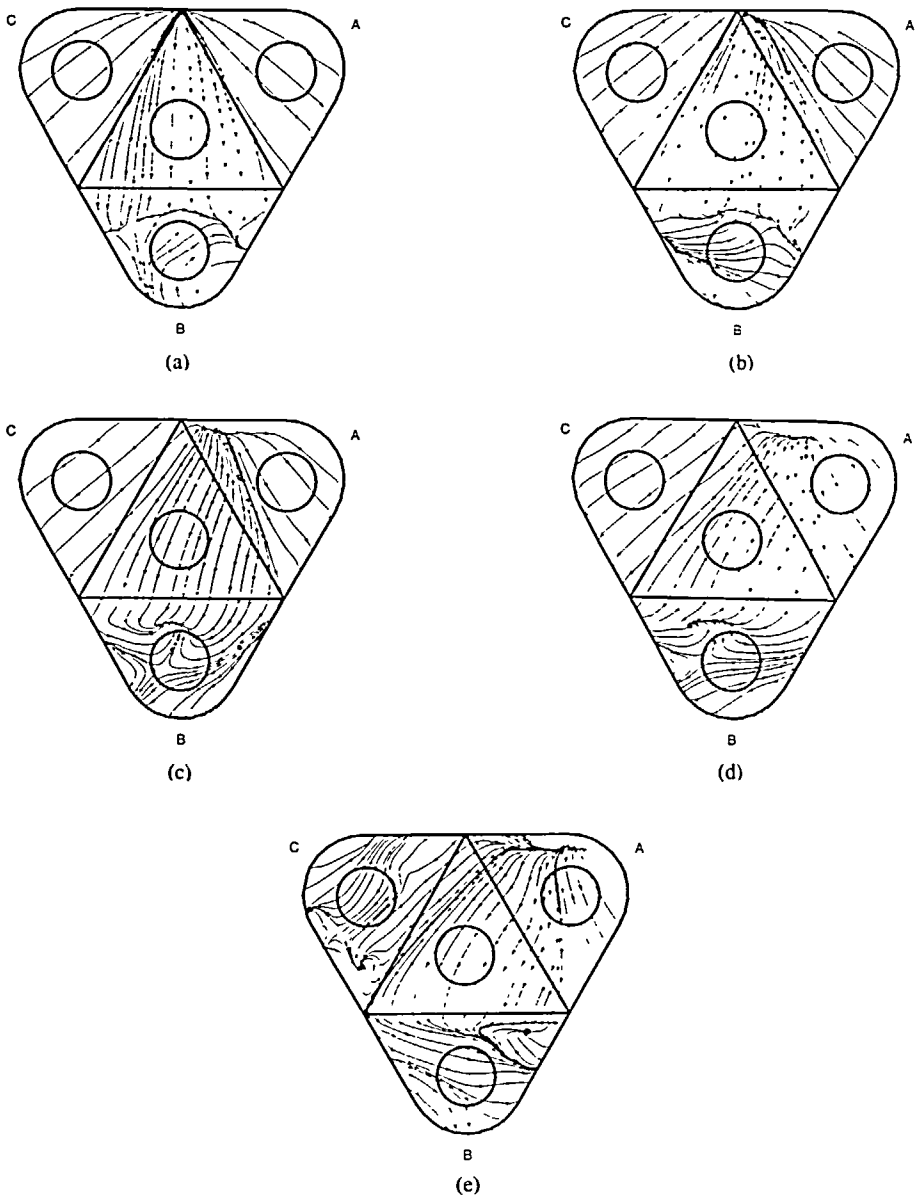

Figure 7 Computational phase portraits. (a) Pitch = 42°, yaw = 0°; (b) pitch = 42°, yaw = 12°; (c) pitch = 42°, yaw = 24°; (d) pitch = 42°, yaw = 36°; (e) pitch = 42°, yaw = 48°

structural bifurcation occurs. At a yaw angle of 48 degrees, *Figure 7e*, the topological features have changed dramatically. The node of attachment or stagnation point is still present. The flow on face *C* is not fully attached anymore, with a node-saddle point combination signalling the presence of global separated flow off this face. On face *B* the detachment node and saddle point have disappeared, replaced with an attachment node. At this high yaw angle the flow at the probe tip comes around from the left of face *B* and flows in the reverse direction to the main flow, going from left to right on the surface of face *B*. The main flow attaches to the right hand

portion of face *B* as seen through the attachment node, but this main flow meets the strongly reversed flow and is forced to change direction.

The preceding phase portraits just presented, *Figures 7a–7e*, illustrate the flow cases used to generate the calibration chart in *Figure 5b*. The flow becomes more complicated as the orientation angles are increased, giving rise to separated flows on the leeward faces, namely face *B* in this case. The discrepancies apparent in the calibration chart, *Figure 5b*, are not very significant. The numerical procedure in these cases seems to have captured the pressure solution very accurately.

As a further guide to visualizing the flow behaviour the three dimensional trajectories of massless particles injected into the flow are shown in *Figure 8* for the case pitch = 42°, yaw = 0°. *Figure 8a* shows the front view of the probe face and *Figure 8b* shows the side view. The streamlines show the fluid flowing smoothly downwards past face *O* and separating at the edge. The exact point of separation is indicated in *Figure 7a*. The recirculating region adjacent to the pressure port at face *B* is seen to be a three dimensional phenomena, with the flow not only swirling in the y–z plane but also in the x–y plane.

Figures 9a, *9b* and *9c* show the computed pressure distribution on the surface of the probe tip for three pitch and yaw cases, keeping the pitch angle at zero degrees while varying the yaw angle. Considering *Figure 9c*, pitch = 0°, yaw = 48°, as a typical example, the stagnation point, as expected, is indicated by the region of highest pressure. The position of the stagnation point corresponds to the nodal point of attachment indicated by the oil streak patterns in *Figure 6e*. There is a pressure decrease going from the windward to the leeward areas. The lowest pressure is apparent just off the edge of the leeward face, face *C*. There seems to be a pressure recovery further down this leeward face. The most striking feature of these diagrams is the large pressure variations across the surface of this pressure probe, across the faces and across the pressure holes themselves. Attached to each figure is an x–y plot showing the extracted data along the line X1–X2 to further highlight the pressure distribution variation. The three symbols represent the experimental data (from the calibration data sets) from the three pressure ports. This x–y plot reveals the amount of sensitivity of the probe pressure response to the geometric design of the probe. It can be seen that the pressure gradients are fairly steep, and the accurate positioning of the pressure ports is critical in getting the desired pressure response, because the smallest misalignment leads to a different pressure reading. These high pressure gradients also create an ambiguity in the computational modelling, since several pressure values are calculated that spans a single pressure tapping, because there are several grid points in each area that a pressure tapping encompasses. These values are simply averaged due to lack of an alternative procedure. The experimental pressure readings of course only gives a single pressure value per tapping. This could be another factor that contributes to the small discrepancies in the calibration chart comparison, *Figure 5*.

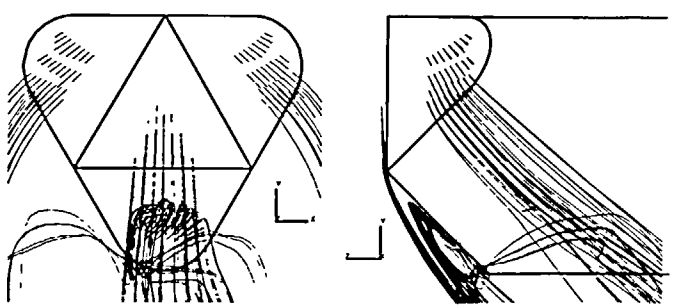

Figure 8 Three-dimensional streamline trajectories (pitch = 42°, yaw = 0°). (a) Front view; (b) side view

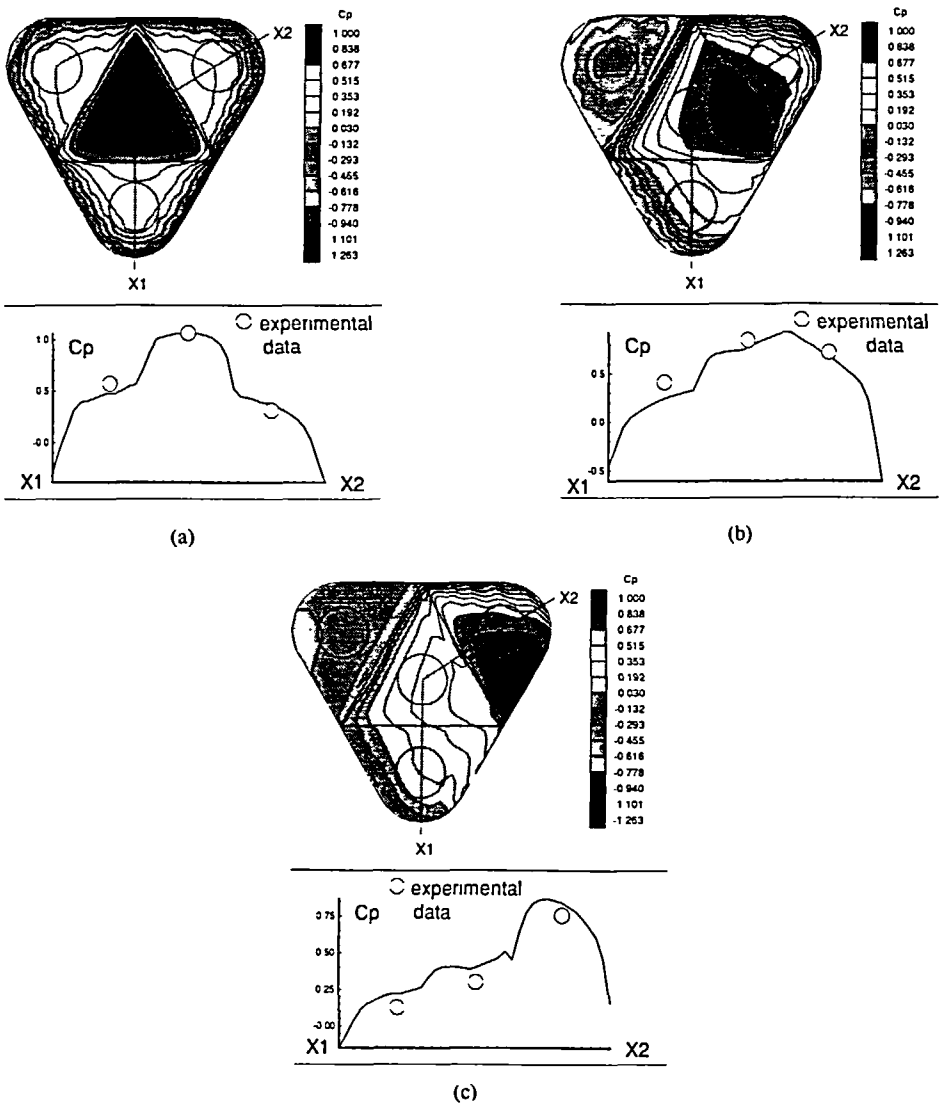

Figure 9 Pressure distribution on probe tip with extracted x–y plot. (a) Pitch = 0°, yaw = 0°; (b) pitch = 0°, yaw = 24°; (c) pitch = 0°, yaw = 48°

The computational oil streak patterns and streamlines have been useful in visualising the flow around the probe tip which has a variety of complicated three dimensional features. The pressure distribution on the probe surfaces have been shown, revealing high pressure gradients that are present. The separation regions on the pressure faces have been clearly identified using topological concepts as the pitch and yaw angles are increased. These complex separation regions might explain some of the discrepancies in the comparison of the calibration data, *Figure 5*. The computational results are perhaps less accurate in these regions, and the pressure solution is affected. On the other hand, the accuracy and reliability of the experimental pressure readings are also affected by the flow separation. All these factors, coupled with the very high pressure gradients present in the probe surfaces, all contribute to the combined errors that are possibly showing up as small discrepancies in the results.

As mentioned in the introduction, an advantage of doing a computational simulation compared to physical experiments is that the flow behaviour at all points in the domain becomes known, not only in discrete areas. An investigation of the flow behaviour around the probe head also reveals some interesting flow phenomena. As seen in *Figure 4*, a way of visualising three-dimensional fluid flow solutions from a numerical simulation is to inject massless particles into the flow and to integrate to obtain the particle trajectories. These serve as three-dimensional streamlines. *Figure 10* shows the top view of the probe head, with the flow visualised by such streamlines. The flow orientation is pitch = 0°, yaw = 0°. The particles were released from points very close to the solid surface of the underside of the probe, with the majority being entrained into the vortex like flow which occurs a short distance away from the angled faces. The particle trajectories indicate that the flow coming from the underside becomes entrained into a region above the probe which recirculates in a fairly large loop. *Figure 11* shows the same situation with the particles released at the top of the probe. The flow goes past the angled faces *A* and *C* and separates off the probe shank. The form of separation is clearly observed as similar to a Werle-type separation[45]. The majority of the near surface flow behaviour at the top of the probe is reversed flow, due to the angled faces which act as ramps to the incoming flow. Some small scale vortices are also present at the top of the probe very near the point where the faces *A* and *C* intersect. A more complex flow pattern that occurs around the probe is shown in *Figure 12*, which illustrates a stable vortex flow phenomena occurring at the leeward side of the probe at pitch = 0°, yaw = 24°. This vortex formation was revealed in the course of the computational investigation. It is a flow feature which is perhaps undesirable with this pressure probe device, which is meant to cause minimum disturbance to the fluid flow as the pressure measurements are being taken. The pressure contours across this vortex is displayed in *Figure 13*. Here one can see clearly the pressure minima at the focus of the vortex, again demonstrating the amount of detail that a computational simulation provides.

The revelation of the separation behaviour, the high pressure gradients on the surface, and the vortex phenomena around the probe demonstrates the usefulness of a computational fluid dynamics investigation. The large variation in the pressure distribution, *Figures 9a–9c*, was not easily inferred from the experimental calibration data, since only the four discrete pressure readings were available (the dots in the extracted x–y plots). Much more detail is acquired in the computed simulation, making a computational approach more suitable for design purposes. The relevant flow variables have been calculated at all points in the domain of interest. It is clearly seen that relocating the position of the pressure tappings will result in a different pressure reading, for example shifting the position of the pressure tappings along line X1–X2 alters the

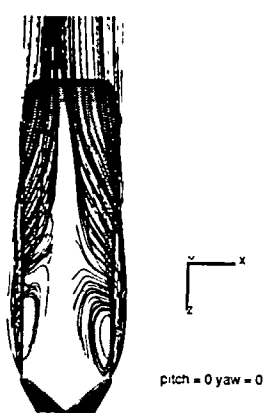

Figure 10 Three-dimensional streamline trajectories started at underside of probe (pitch = 0°, yaw = 0°)

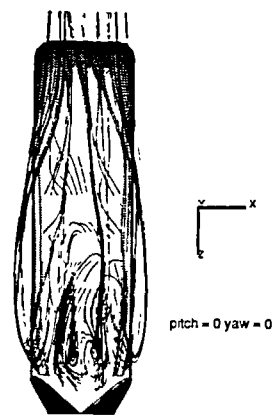

Figure 11 Three-dimensional streamline trajectories started at top of probe (pitch = 0°, yaw = 0°)

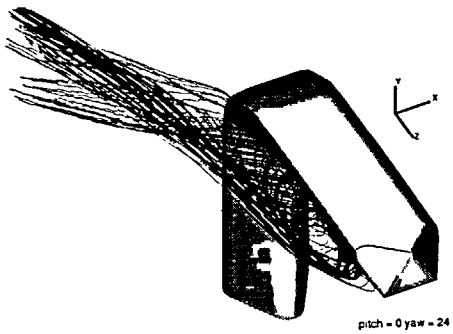

Figure 12 Three-dimensional streamline trajectories showing vortex (pitch = 0°, yaw = 24°)

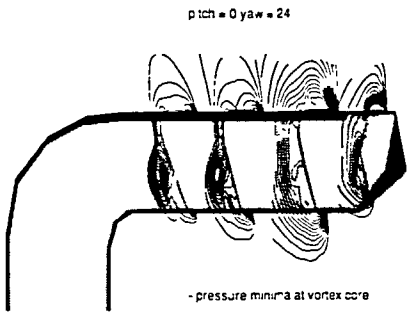

Figure 13 Pressure contours across the vortex (pitch = 0°, yaw = 24°)

pressure value. This then will yield slightly different calibration surfaces (or curves). Whether it is possible to produce a better probe design (by shifting the positions of the tappings and/or varying the geometry of the probe) can now be investigated, quite efficiently, by using this computational approach. It is a simple matter of varying the relevant geometry features and boundary conditions and seeing the corresponding flow solutions. A better probe design could possibly incorporate more easily interpolated calibration surfaces, more reliable measurements, and better resolution at higher pitch/yaw angles. It might also incorporate less disturbance to the flow being measured. Building experimental prototypes is a more expensive method of achieving this task. Clearly, in the area of engineering design, a computational approach gives one the capability to produce optimal designs efficiently, and the Cobra probe is only one example of such an apparatus that can be optimized.

CONCLUSIONS

The detailed flow around a multi-hole pressure probe has been studied from a computational viewpoint. The three-dimensional separated flow behaviour at the probe tip has been described, showing the topological features of the flow as the pitch and yaw orientation angles of the probe are varied. Separated flow occurring at the leeward faces for certain angles of pitch and yaw are visualised using computational oil streak patterns. The calculated surface pressure distribution reveals steep pressure gradients at the probe tip adjacent to the pressure tappings. Numerically integrated three-dimensional streamlines visualised the flow patterns around the probe head, showing separated flow behaviour at the sides of the heat probe, and vortex formation in the leeward side of the probe shank.

The computational results based on the Navier–Stokes equations compare favourably with experimental results. The accuracy of the numerical computations have been validated quantitatively using experimental calibration data, and qualitative comparisons using preliminary oil film visualisation results have been favourable. The finite volume code RANSTAD is therefore suitable for solving the flow behaviour around the four-hole Cobra pressure probe. Comparison using the calibration charts demonstrate the capability of the numerical calculations as a useful method of verifying experiments, and generating computational calibration results for proposed designs in a time efficient manner. Computational flow visualisation results and pressure distributions demonstrate the profiency of the numerical simulation in undertaking detailed studies of complex flow devices for analysis and design purposes. Improved or optimal apparatus designs are feasible using this computational approach, and are economically viable.

ACKNOWLEDGEMENT

The first author works under the support of an Australian Postgraduate Research Award and a scholarship from CSIRO Division of Mineral and Process Engineering.

REFERENCES

1 Jameson, A. *Science*, **245**, 361–371 (1989)
2 Patankar, S. V. *Numerical Heat Transfer and Fluid Flow*, Hemisphere (1980)
3 Durst, F., Melling, A. and Whitelaw, J. H. *Principles and Practice of Laser-Doppler Anemometry*, Academic Press, New York (2nd Ed.) (1981)
4 Musgrove, A. R., Hooper, J. D., Maher, K. J. and Davidson, M. R. LDV measurements of the turbulence field in a gas-agitated water bath, *Second World Conf. on Exp. Heat Trf. Fluid Mech. and Thermodynam.*, Dubrovnik, Yugoslavia (1991)
5 Shepherd, I. C., LaFontaine, R. F., Welch, L. W., Soria, J. and Pearson, I. G. Measurements of instantaneous flows using particle image velocimetry, *Second World Conf. on Exp. Heat Trf., Fluid Mech. and Thermodynam.*, Dubrovnik, Yugoslavia (1991)
6 Shepherd, I. C. and LaFontaine, R. F. Mapping instantaneous velocity fields using particle image velocimetry, *11th Australasian Fluid Mechanics Conference, Hobart, Australia* (1992)
7 Perry, A. E. *Hot-wire Anemometry*, Clarendon Press, Oxford (1982)
8 Hooper, J. D. Fully Developed Turbulent Flow Through A Rod Cluster, *PhD Thesis*, University of New South Wales, Sydney (1980)
9 Bryer, D. W. and Pankhurst, R. C. *Pressure-probe Methods for Determining Wind Speed and Flow Direction*, HMSO (1971)
10 Wright, M. A. The evaluation of a simplified form of presentation for five-hole spherical and hemispherical pitometer calibration data, *J. Phys. E: Sci. Instrum.*, **3**, 356–362 (1970)
11 Judd, A. M. Calibration of a five tube probe for measuring wind speed and direction, *J. Phys. E: Sci. Instrum.*, **8**, 115–116 (1975)
12 Everett, K. N., Gerner, A. A. and Durston, D. A. Seven-hole cone probes for high angle flow measurement: theory and calibration, *AIAA J.*, **21**, 992–998 (1983)
13 Ligrani, P. M., Singer, B. A. and Baun, L. R. Miniature five-hole pressure probe for measurement of three mean velocity components in low-speed flows, *J. Phys. E: Sci. Instrum.*, **22**, 868–876 (1989)
14 Holmes, J. D. and Lewis, R. E. Optimisation of dynamic pressure measurement systems I. Single point measurements, *J. of Wind Engng. and Ind. Aerodyn.*, **25**, 249–273 (1987)
15 Hooper, J. D., Musgrove, A. R. de L. and Smith, B. Pressure probe measurements of the mean and turbulent structure of a swirling jet, *11th Australasian Fluid Mech. Conf.*, Hobart, Australia (December 1992)
16 Shepherd, I. C. A four-hole pressure probe for fluid flow measurements in three dimensions, *J. Fluids Eng.*, **103**, 590–594 (1981)
17 Hooper, J. D. and Musgrove, A. R. de L. Multi-hole pressure probes for the determination of the total velocity vector in turbulent single-phase flow, *4th Int. Symp. on Transport Phenomena*, ISTP-IV (Ed. J. A. Reizes), Sydney (1991)
18 Fletcher, C. A. J. Computational modelling of complex industrial flows, *4th Int. Symp. on Transport Phenomena in Heat and Mass Transfer*, (Ed. J. A. Reizes), Elsevier, 839–850 (1992)
19 Rodi, W. *Turbulence Models and Their Application in Hydraulics*, IAHR, Delft (1980)
20 Armfield, S. W., Cho, N.-H. and Fletcher, C. A. J. *AIAA J.*, **28**, 453–460 (1990)
21 Cho, N.-H., Fletcher, C. A. J. and Srinivas, K. Efficient computation of wing body flows, *12th Int. Conf. Num. Meth. Fluid Dynamics*, Oxford, UK (1990)
22 Bar-Yoseph, P. and Fletcher, C. A. J. *On Continuum Modelling of Gas-Solid Flows with Application to Erosion Prediction*, Dept. of Mechanical Eng. Report, University of Sydney (1991)
23 Thompson, J. F., Warsi, Z. U. A. and Wayne Mastin, C. *Num. Grid Generation*, North-Holland (1985)
24 Fletcher, C. A. J. *Computational Techniques for Fluid Dynamics*, Springer-Verlag, 2nd Edn. (1991a)
25 Van Doormal, J. P. and Raithby, G. D. Enhancements for the SIMPLE method for predicting incompressible fluid flow, *Num. Heat Transfer.*, **7**, 147–163 (1984)
26 Rhie, C. M. and Chow, W. L. Numerical study of turbulent flow past an airfoil with trailing edge separation, *AIAA J.*, **21**, 11, 1525–1532 (1983)
27 Eriksson, L.-E. Flow solution on a dual-block grid around an airplane, *Comput. Meths. Appl. Mech. Eng.* **64**, 79–93 (1987)
28 Smith, R. E. and Eriksson, L.-E. Algebraic grid generation, *Comput. Meths. Appl. Mech. Eng.* **64**, 285–300 (1987)
29 Chang, I. S. Three-dimensional, two-phase supersonic nozzle flows, *AIAA J.*, **21**, 671 (1983)
30 Chen, B. C.-J., Chien, T. H., Sha, W. T. and Kim, J. H. 3-D solution of flow in an infinite square array of circular tubes by using boundary-fitted coordinate systems, *Num. Grid Generation* (Ed. J. F. Thompson), North-Holland (1982)

31 Holst, T. and Thomas, S. Numerical solution of transonic wing flow fields, *AIAA J.*, **21**, 863 (1983)
32 Warsi, Z. U. A. Basic differential models for coordinate generation, *Num. Grid Generation* (Ed. J. F. Thompson), North-Holland (1982)
33 Eiseman, P. R. A multi-surface method of coordinate generation, *J. Comp. Phys.*, **33**, 118–150 (1979)
34 Kahaner, D., Moler, C. and Nash, S. *Numerical Methods and Software*, Prentice-Hall (1989)
35 Kennon, S. R. and Dulikravich, G. S. Generation of computational grids using optimization, *AIAA J.*, **24**, 1069–1073 (1986)
36 Thompson, J. F. Grid generation techniques in computational fluid dynamics, *AIAA J.*, **22**, 1505–1523 (1984)
37 Forsey, C. R. An extension of a transonic wing/body code to include underwing pylon/nacelle effects, *AIAA Paper 83-1805*, Danvers, Mass. (1983)
38 Jameson, A. and Baker, T. J. Solution of the Euler equations for complex configurations, *AIAA Paper 83-1929*, Danvers, Mass. (1983)
39 Steger, J. L. and Benek, J. A. On the use of composite grid schemes in computational aerodynamics, *Comput. Meths. Appl. Mech. Eng.*, **64**, 301–320 (1987)
40 Merzkirch, W. *Flow Visualization*, Academic Press (1987)
41 Tan, A. *Private Communication* (1993)
42 Perry, A. E. and Chong, M. S. A description of eddying motions and flow patterns using critical point concepts, *Ann. Rev. Fluid Mech.*, **19**, 125–155 (1987)
43 Tobak, M. and Peake, D. J. Topology of three-dimensional separated flows, *Ann. Rev. Fluid Mech.*, **14**, 61–85 (1982)
44 Chapman, G. T. and Yates, L. A. Topology of flow separation on three-dimensional bodies, *Appl. Mech. Rev.*, **44**, 7, 329–345 (1991)
45 Yates, L. A. and Chapman, G. T. Streamlines, vorticity lines, and vortices around three-dimensional bodies, *AIAA J.*, **30**, 7, 1819–1826 (1992)